

# Simulation of electromagnetic signals propagating through magnetoplasma

Kalpana Singh\* and R. P. Singh

Department of Physics, Banaras Hindu University, Varanasi 221 005, India

**We have developed a simulation technique to obtain the dynamic spectra of electromagnetic signals propagating through an inhomogeneous magnetoplasma. The Maxwell's equations and equation of motion are solved to determine the expression for wave fields. By expressing the excitation source in terms of Dirac delta function, the exact frequency–time dependence of the propagating non-monochromatic signal is computed for different magnetoplasma models. The results are further used to obtain the dynamic spectra of whistler mode waves propagating through different regions of the terrestrial magnetosphere, which have wide applications in the diagnostics of magnetospheric parameters. It is interesting to observe that the technique used under various conditions simultaneously explains low dispersion whistlers, nose whistlers, precursors and proton whistlers. Finally, we attempt to explain whistler mode waves observed particularly at low latitude Indian ground stations.**

THE return stroke of lightning discharge is known to generate electromagnetic signals in wide frequency range in all directions. Part of the signal energy is reflected back from the ionosphere and propagates in the space between the earth and the ionosphere, while a part of the signal energy penetrates the ionosphere and propagates in the magnetosphere along the geomagnetic field lines in a very low frequency (VLF) band ( $\omega \ll \omega_b$ , where  $\omega$  is the signal frequency and  $\omega_b$  is the electron gyro frequency) with little attenuation. These naturally occurring, right circularly polarized waves in low frequency range ( $\omega \ll \omega_b$ ) called whistlers provide a powerful ground-based technique for probing the magnetosphere<sup>1</sup>. The analysis of dispersion of these radio signals in the audio frequency range that 'whistle', yield information about the medium parameters such as electron density, total electron content of a flux tube, electron temperature, magnetic field and large-scale convective electric fields in the magnetosphere<sup>2</sup>.

Whistler mode waves were first observed by telephone operators during the First World War<sup>3</sup>, and subsequently studied by Eckersley<sup>4</sup> and Barkhausen<sup>5</sup>. Storey<sup>6</sup> made systematic observations and explained various features using magnetoionic theory of wave propagation. Since then, huge amount of data concerning whistler waves and related

VLF emissions is available mostly from mid- and high-latitude regions<sup>7,8</sup>. Relevant data from low-latitude regions are meagre and mostly come from Indian and Japanese stations<sup>1,9</sup>. The rate of whistler occurrence is quite low at low latitudes, although the thunderstorm activity is quite high near the equatorial region, which is the natural source of VLF waves in the space plasma<sup>1,10,11</sup>. Whistler occurrence at low latitudes is controlled by the presence of fewer ducts, curved geomagnetic field lines, plasma inhomogeneities and attenuation/amplification of waves during propagation from the source to the observation point.

The VLF waves received on the earth's surface propagate along the geomagnetic field lines. Amplitude measurements at the conjugate points showed that VLF waves propagate almost without attenuation. The propagation mode at the mid- and high-latitudes is ducted mode, whereas at low latitudes it is non-ducted, pro-longitudinal mode<sup>1</sup>. Ohta *et al.*<sup>12</sup>, using three-dimensional ray tracing for the realistic ionospheric/magnetospheric model, had shown that whistler-mode waves at low latitudes could propagate parallel to the geomagnetic field lines without appreciable attenuation and one can easily observe one-hop and three-hop whistlers.

Signals propagating at finite angle to the magnetic field suffer a large attenuation and hence are dissipated in the magnetosphere. However, VLF waves can propagate in longitudinal mode and get dispersed because of frequency dependence of their group velocity. In magnetized (anisotropic) plasma, we considered longitudinal propagation of VLF non-monochromatic waves, which exhibit a characteristic dispersion. Moreover, group velocity further depends upon the plasma density and magnetic field strength of the ambient medium. In order to explain the shapes of the signal on spectrograms, earlier workers have either used approximations<sup>13</sup> or different extension methods were applied using the results of the monochromatic solution<sup>14,15</sup>. None of these studies could account for complete and precise determination of the space–time functions of the electric and magnetic field strengths resulting from an arbitrary excitation source.

In this article, we present the full wave analysis<sup>16</sup> to derive the whistler-mode signal propagating longitudinally through a one-dimensional, inhomogeneous, weakly ionized magnetoplasma, in which wave energy dispersion is caused by interaction between electrons and wave fields, and dissipation of energy is caused by collisions between electrons

\*For correspondence. (e-mail: kalpanasingh@myself.com)

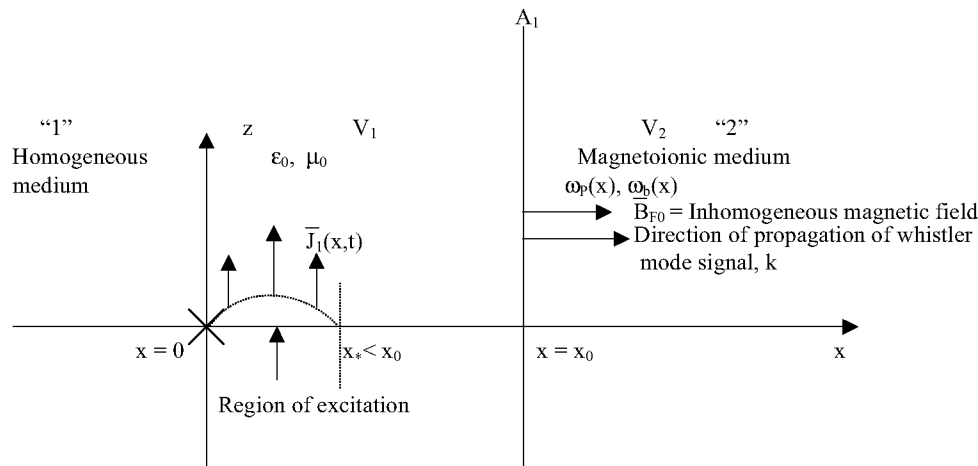


**Figure 1.** Schematic model used in computation of whistler-mode wave propagating through inhomogeneous magnetoplasma.

and neutrals. The Maxwell's equations, continuity equation and equation of motion are used to develop the appropriate wave equation, which is solved by using the technique of Laplace transformation. In consequence, we obtain the expressions for electric and magnetic fields as a function of frequency and time for a given source current. We consider weakly inhomogeneous magnetoplasma in which electron density and magnitude of the magnetic field of the ambient medium are considered to vary gradually in space and this variation is taken along the direction of propagation of the wave, which is also the direction of the magnetic field (Figure 1). In the present formulation, only the magnitude of the external magnetic field is assumed to vary during wave propagation, however, variation in the direction of the magnetic field is not taken into account.

Here, a simulation technique has been developed to compute numerically the whistler-mode signal as a function of space, time and frequency for a given model of magnetoplasma, with special reference to the terrestrial magnetosphere. We discuss some of the properties of recorded whistler-mode waves at the ground-based Indian stations located at different latitudes and longitudes. Further, the effect of variation of collision frequency on the spectra of the observed whistlers at low-latitude stations is studied.

In addition, the dynamic spectrum of the whistlers recorded at mid- and high latitudes usually contains the nose frequency, at which the group delay time of whistler propagation is minimal, whereas the nose frequency does not appear on the spectrogram of whistlers observed at low-latitude stations. At low latitudes, nose frequency is of the order of 100 kHz, which cannot be observed at the ground station due to high attenuation at such a high frequency, because the attenuation of VLF waves propagating through the ionosphere is minimum for wave frequencies  $\sim 5$  kHz and it increases as wave frequency increases or decreases. However, the nose frequency is an important element in whistler analysis, especially in the determination

of the path of propagation. The present technique yields complete spectrum, including nose frequency and hence is quite useful in probing. Because with the known nose extension techniques, calculation of nose frequency is possible but the error introduced in the estimation is quite large.

Further, one of the interesting and intriguing naturally occurring VLF phenomena is that of whistler precursors, discrete VLF emissions which are observed before the whistlers with which they appear to be associated. Precursors appear on frequency-time spectrograms as rising tones. When the signal partly reflected from the equatorial region is received on the earth's surface, it resembles a one-hop whistler. If the gap between the spectra of one-hop whistler and precursor is very small, then both may combine and we get spectra closely resembling hooks. Simulation of the precursor is another important feature of the work presented; the dynamic spectrum of precursors could not be properly explained otherwise. The spectrum of the precursor is numerically computed by considering parametric reflection of parallel propagating whistler-mode waves when wave frequency becomes equal to the lower hybrid resonance frequency. The latter is geomagnetic field and plasma density dependent. The waves are parametrically reflected from two points located before and after the equator.

Here, we also replicated proton whistlers that are electromagnetic waves observed in the ionosphere, as a rising tone following short fractional-hop electron whistlers and that asymptotically approaches the proton frequency at the satellite. Proton whistlers are mostly detected in the altitude range 1000–2000 km by satellite-borne VLF receivers<sup>17</sup>. They are the dispersed forms of the original lightning impulse that propagates as left-hand polarized ion-cyclotron waves. The dispersion arises from the effects of ions on the wave propagation in the ionosphere, and therefore, hydrogen ion concentration, electron density and proton gyrofrequency can be determined from the dispersion analysis of

proton whistlers. The proton whistlers are simulated considering propagation of non-monochromatic signal through multi-component plasma existing in the ionosphere/inner plasmasphere. Earlier proton whistlers are explained by considering polarization reversal of the right-hand polarized signal into the left-hand polarized signal at the crossover frequency in the upper ionosphere.

### Theoretical formalism

We consider a transient current source in plasma-free medium, which generates wide spectrum of electromagnetic fields. These waves while propagating through the plasma medium interact with the electrons and ions present there. The Maxwell's equations govern the propagation of the wave, whereas the coupling of wave field with the medium is governed by the momentum and continuity equations. These equations are solved in closed form to obtain the expression for wave fields.

In the derivation of wave fields, we consider the source of signal (lightning discharge) to lie in region '1' as shown in Figure 1, in which the plasma is absent and hence medium '1' has no significant interaction with the signal. Figure 1 shows the location of excitation inside the half-space '1', i.e.,  $0 \leq x \leq x_*$  during the time interval  $0 \leq t \leq t_0$ ; where  $x_* \leq x_0$ ,  $x_0$  being the boundary surface separating the free space and plasma medium. The direction of excitation or source current is taken parallel to the  $z$ -axis, i.e.  $\bar{J}_1(x, t) = J_0(x, t)\hat{e}_z$ . The medium '2' is supposed to be an infinite half space embedded by the magnetoplasma.

The plasma density and dc magnetic field are considered to vary in the  $x$ -direction, while collision frequency ( $\nu_c$ ) is taken to be independent of space. The interaction of signal with the plasma medium is governed by the equation of motion and Maxwell's equations, which form a close set of equations. The velocity of the charged particle  $\bar{v}$  is governed by the momentum equation:

$$m \frac{\partial \bar{v}}{\partial t} + m \nu_c \bar{v} = q(\bar{E} + \bar{v} \times \bar{B}), \quad (1)$$

where  $B = B_{F0} + B_1(r, t)$ ,  $B_{F0}$  is the steady state magnetic field taken to be in the  $x$ -direction,  $E(r, t)$  and  $B_1(r, t)$  are the electric and magnetic fields of the wave. In general,  $|B_1| \ll |B_{F0}|$  and hence it is neglected. Writing eq. (1) in component form and following the procedure of Kamke<sup>18,19</sup>, we obtain the solution in the following form:

$$v_x = e^{-\nu_c t} \left[ C + \int_t^q \frac{q}{m} E_x(\tau) e^{\nu_c \tau} d\tau \right], \quad (2)$$

$$v_y = e^{-\nu_c t} (C_1 \cos \omega_b t + C_2 \sin \omega_b t) + \frac{1}{\omega_b} \int \varphi_y(\tau) e^{-\nu_c(t-\tau)} \sin \omega_b(t-\tau) d\tau, \quad (3)$$

$$v_z = e^{-\nu_c t} (C_1 \cos \omega_b t + C_2 \sin \omega_b t) + \frac{1}{\omega_b} \int \varphi_z(\tau) e^{-\nu_c(t-\tau)} \sin \omega_b(t-\tau) d\tau, \quad (4)$$

where

$$\varphi_y(\tau) = \frac{q}{m} [E'_y(\tau) + \nu_c E_y(\tau) - \omega_b E_z(\tau)],$$

$$\varphi_z(\tau) = \frac{q}{m} [E'_z(\tau) + \nu_c E_z(\tau) + \omega_b E_y(\tau)].$$

The homogeneous terms of the above equations do not contain the contribution from the excitation source and hence they are not real signals. Therefore, these parts will be eliminated in the computation of current. Substituting the expression for velocity components, the expressions for current components are obtained as,

$$J_x = q N v_x = \epsilon_0 \omega_p^2 e^{-\nu_c t} \left[ \int_t E_x(\bar{r}, \tau) e^{\nu_c \tau} d\tau \right], \quad (5)$$

$$J_y = \epsilon_0 \omega_p^2 \left\{ \frac{1}{\omega_b} \int \frac{\partial E_y}{\partial \tau} e^{-\nu_c(t-\tau)} \sin \omega_b(t-\tau) d\tau + \frac{1}{\omega_b} \nu_c \int E_y e^{-\nu_c(t-\tau)} \sin \omega_b(t-\tau) d\tau - \int E_z e^{-\nu_c(t-\tau)} \sin \omega_b(t-\tau) d\tau \right\}, \quad (6)$$

$$J_z = \epsilon_0 \omega_p^2 \left\{ \frac{1}{\omega_b} \int \frac{\partial E_z}{\partial \tau} e^{-\nu_c(t-\tau)} \sin \omega_b(t-\tau) d\tau + \frac{1}{\omega_b} \nu_c \int E_z e^{-\nu_c(t-\tau)} \sin \omega_b(t-\tau) d\tau + \int E_y e^{-\nu_c(t-\tau)} \sin \omega_b(t-\tau) d\tau \right\}. \quad (7)$$

Substituting the above equations into Maxwell's equations,

$$\bar{\nabla} \times \bar{H} = \bar{J} + \epsilon_0 \frac{\partial \bar{E}}{\partial t} \quad \text{and} \quad \bar{\nabla} \times \bar{E} = -\mu_0 \frac{\partial \bar{H}}{\partial t},$$

we obtain the following differential equations:

$$\frac{\partial H_z}{\partial y} - \frac{\partial H_y}{\partial z} = \epsilon_0 \left\{ \omega_p^2 e^{-\nu_c t} \int E_x(\bar{r}, \tau) e^{\nu_c \tau} d\tau + \frac{\partial E_x}{\partial t} \right\},$$

$$\left. \begin{aligned} \frac{\partial H_x}{\partial z} - \frac{\partial H_z}{\partial x} &= \epsilon_0 \left\{ \frac{\omega_p^2}{\omega_b} \int_t^t \frac{\partial E_y}{\partial \tau} e^{-\nu_c(t-\tau)} \sin \omega_b(t-\tau) d\tau \right. \\ &\quad + \frac{\omega_p^2}{\omega_b} \nu_c \int_t^t E_y e^{-\nu_c(t-\tau)} \sin \omega_b(t-\tau) d\tau \\ &\quad \left. - \omega_p^2 \int_t^t E_z e^{-\nu_c(t-\tau)} \sin \omega_b(t-\tau) d\tau + \frac{\partial E_y}{\partial t} \right\}, \\ \frac{\partial H_y}{\partial x} - \frac{\partial H_x}{\partial y} &= \epsilon_0 \left\{ \frac{\omega_p^2}{\omega_b} \int_t^t \frac{\partial E_z}{\partial \tau} e^{-\nu_c(t-\tau)} \sin \omega_b(t-\tau) d\tau \right. \\ &\quad + \frac{\omega_p^2}{\omega_b} \nu_c \int_t^t E_y e^{-\nu_c(t-\tau)} \sin \omega_b(t-\tau) d\tau \\ &\quad \left. + \omega_p^2 \int_t^t E_y e^{-\nu_c(t-\tau)} \sin \omega_b(t-\tau) d\tau + \frac{\partial E_z}{\partial t} \right\}. \end{aligned} \right\} \quad (8)$$

$$\left. \begin{aligned} \frac{\partial E_z}{\partial y} - \frac{\partial E_y}{\partial z} &= -\mu_0 \frac{\partial H_x}{\partial t}, \\ \frac{\partial E_x}{\partial z} - \frac{\partial E_z}{\partial x} &= -\mu_0 \frac{\partial H_y}{\partial t}, \\ \frac{\partial E_y}{\partial x} - \frac{\partial E_x}{\partial y} &= -\mu_0 \frac{\partial H_z}{\partial t}. \end{aligned} \right\} \quad (9)$$

Taking time derivative of eq. (8) and using eq. (9), we obtain

$$\frac{1}{c^2} \left( \omega_p^2 E_x + \frac{\partial^2 E_x}{\partial t^2} \right) = 0. \quad (10)$$

Equation (10) describes plasma oscillations and hence for a plane wave signal propagating in the  $x$ -direction, we consider  $E_x \equiv 0$ , and  $\frac{\partial}{\partial y} = \frac{\partial}{\partial z} \equiv 0$ .

The remaining electric field components are obtained as:

$$\begin{aligned} \frac{\partial^2 E_y}{\partial x^2} &= \frac{1}{c^2} \left\{ \omega_p^2(x) \int_0^t \frac{\partial E_y}{\partial \tau} e^{-\nu_c(t-\tau)} \cos \omega_b(x)(t-\tau) d\tau + \nu_c \omega_p^2(x) \right. \\ &\quad \left. \int_0^t E_y(\tau) e^{-\nu_c(t-\tau)} \cos \omega_b(x)(t-\tau) d\tau - \omega_b(x) \omega_p^2(x) \right. \\ &\quad \left. \int_0^t E_z(\tau) e^{-\nu_c(t-\tau)} \cos \omega_b(x)(t-\tau) d\tau + \frac{\partial^2 E_y}{\partial t^2} \right\}, \end{aligned} \quad (11)$$

$$\begin{aligned} \frac{\partial^2 E_z}{\partial x^2} &= \frac{1}{c^2} \left\{ \omega_p^2(x) \int_0^t \frac{\partial E_z}{\partial \tau} e^{-\nu_c(t-\tau)} \cos \omega_b(x)(t-\tau) d\tau + \nu_c \omega_p^2(x) \right. \\ &\quad \left. \int_0^t E_z(\tau) e^{-\nu_c(t-\tau)} \cos \omega_b(x)(t-\tau) d\tau + \omega_b(x) \omega_p^2(x) \right. \\ &\quad \left. \int_0^t E_y(\tau) e^{-\nu_c(t-\tau)} \cos \omega_b(x)(t-\tau) d\tau + \frac{\partial^2 E_z}{\partial t^2} \right\}, \end{aligned} \quad (12)$$

where the wave is assumed to be propagating along the  $x$ -direction. To solve the above differential equation, the method of Laplace transform is applied only for  $t \rightarrow s$  transformation and not for  $x \rightarrow p$  transformation, because angular gyrofrequency  $\omega_b(x)$  and angular plasma frequency  $\omega_p(x)$  are arbitrary functions of  $x$  due to the inhomogeneity of the magnetospheric plasma.

In deriving the above equations, generality of the solution is retained by considering the excitation at  $t = 0$ , so that at  $t \leq 0$  there is no signal in the plasma. Thus the following initial conditions are satisfied:

$$\begin{aligned} E_y(x, t=0) &= e_{yx0}(x) = 0; \quad \left. \frac{\partial E_y(x, t)}{\partial x} \right|_{x=0} = e'_{y0t}(t) = 0, \\ E_y(x=0, t) &= e_{y0t}(x) = 0; \quad \left. \frac{\partial E_y(x, t)}{\partial t} \right|_{t=0} = \dot{e}_{yx0}(x) = 0. \end{aligned}$$

For a weak or quasi-inhomogeneous medium, W.K.B. method of solution is applied, where the propagation factor given for homogeneous plasma forms the basis of the inhomogeneous solution<sup>20,21</sup>. This implies that if  $P_i$  is a pole and solution of wave field then,

$$e^{p(s)x} \xrightarrow{(s \leftrightarrow j\omega)} e^0 \int_0^x p(x, s) dx.$$

The Laplace transform of eqs (11) and (12) after using the above boundary conditions reduces to,

$$c^2 p^2 E_y(p, s) = \left[ \omega_p^2(x) \frac{(s + \nu_c)^2}{(s + \nu_c)^2 + \omega_b^2(x)} + s^2 \right] \quad (13)$$

$$E_y(p, s) - \omega_p^2(x) \omega_b(x) \frac{(s + \nu_c)}{(s + \nu_c)^2 + \omega_b^2(x)} E_z(p, s)$$

and

$$\begin{aligned} c^2 p^2 E_z(p, s) &= \left[ \omega_p^2(x) \frac{(s + \nu_c)^2}{(s + \nu_c)^2 + \omega_b^2(x)} + s^2 \right] \\ E_z(p, s) + \omega_p^2(x) \omega_b(x) \frac{(s + \nu_c)}{(s + \nu_c)^2 + \omega_b^2(x)} E_y(p, s) \end{aligned} \quad (14)$$

$$E_y(p, s) + c^2 [p e_{z0t}(s) + e'_{z0t}(s)].$$

where  $e'_{z0t}(s)$  is Laplace transformed form of  $\frac{\partial E_z(x,t)}{\partial x} \Big|_{x=0}$ .

Rearranging the above equations, poles are obtained as<sup>22</sup>,

$$p_{1,2,3,4}(x,s) = \pm \frac{1}{c} \sqrt{\frac{\omega_p^2(x)[s+v_c]^2 + s^2[\{s+v_c\}^2 + \omega_b^2(x)] \pm j\omega_p^2(x)\omega_b(x)[s+v_c]}{[s+v_c]^2 + \omega_b^2(x)}} \quad (15)$$

Equation (15) represents four poles leading to four waves in the medium. Substituting  $s = j\omega$ , the four poles are rewritten as

$$p_{1,2} = \pm \frac{1}{c} j \sqrt{\frac{\omega^2(\omega_p^2 + \omega_b^2 - \omega^2) + \omega\omega_b\omega_p^2}{\omega_b^2 - \omega^2}} \sqrt{\frac{1 - \frac{v_c^2(\omega_b^2 - \omega^2) + jv_c[2\omega(\omega_p^2 - \omega^2) + \omega_p^2\omega_b]}{\omega_p^2\omega_b\omega + \omega^2(\omega_p^2 + \omega_b^2 - \omega^2)}}{1 + \frac{v_c^2 + 2j\omega v_c}{\omega_b^2 - \omega^2}}} \quad (16)$$

$$p_{3,4} = \mp \frac{1}{c} \sqrt{\frac{(\omega\omega_b\omega_p^2 + \omega^4) - \omega^2(\omega_p^2 + \omega_b^2)}{\omega_b^2 - \omega^2}} \sqrt{\frac{1 + \frac{v_c^2(\omega_b^2 - \omega^2) + jv_c[2\omega(\omega_p^2 - \omega^2) + \omega_p^2\omega_b]}{(\omega\omega_b\omega_p^2 + \omega^4) - \omega^2(\omega_p^2 + \omega_b^2)}}{1 + \frac{v_c^2 + 2j\omega v_c}{\omega_b^2 - \omega^2}}}$$

where  $\omega_b$  and  $\omega_p$  are space-dependent.

The field components, corresponding to poles  $p_1$  and  $p_2$ , belong to whistler-mode signal. This is verified by deriving the polarization of the signal where we obtain,  $E_y(x,s) = jE_z(x,s)$ . Thus, the complete expression for  $E_y(x,s)$  is obtained as<sup>22</sup>,

$$E_y(x,s) = \frac{c^2 a_0(x,s) a_\infty(x,s) a_2(s)}{b_3(x,s)} \left\{ \frac{\left[ p_1(x,s) + \frac{a_1(s)}{a_2(s)} \right]}{[p_1^2(x,s) - p_3^2(x,s)][p_1(x,s) - p_2(x,s)]} e^{\int_0^x p_1(x,s) dx} - \frac{\left[ -p_1(x,s) + \frac{a_1(s)}{a_2(s)} \right]}{[p_1^2(x,s) - p_3^2(x,s)][p_1(x,s) - p_2(x,s)]} e^{-\int_0^x p_1(x,s) dx} \right\} \quad (17)$$

In the above, we clearly see that there are two components of  $E_y$ , one propagating in the forward direction and the other is the reflected signal propagating in the opposite direction. Similarly,  $E_z$  also has two components and is obtained as:

$$E_z(x,s) = \frac{c^2 a_\infty(x,s) a_4(x,s) a_2(s)}{b_3(x,s)} \left\{ \frac{\left[ p_1(x,s) + \frac{a_1(s)}{a_2(s)} \right] \left[ p_1^2(x,s) - \frac{a_3(x,s)}{a_4(x,s)} \right]}{[p_1^2(x,s) - p_3^2(x,s)][p_1(x,s) - p_2(x,s)]} e^{\int_0^x p_1(x,s) dx} - \frac{\left[ -p_1(x,s) + \frac{a_1(s)}{a_2(s)} \right] \left[ p_1^2(x,s) - \frac{a_3(x,s)}{a_4(x,s)} \right]}{[p_1^2(x,s) - p_3^2(x,s)][p_1(x,s) - p_2(x,s)]} e^{-\int_0^x p_1(x,s) dx} \right\} \quad (18)$$

where  $a_i$  and  $b_i$  used in eqs (17) and (18) are given below:

$$a_0(x,s) = -\omega_b(x)\omega_p^2(x)[s+v_c],$$

$$a_\infty(x,s) = [s+v_c]^2 + \omega_b^2(x),$$

$$a_1(s) = e'_{z0t}(s) = B(s), \quad a_2(s) = e_{z0t}(s) = A(s),$$

$$a_3(x,s) = \omega_p^2(x)[s+v_c]^2 + s^2([s+v_c]^2 + \omega_b^2(x)),$$

$$a_4(x,s) = \{[s+v_c]^2 + \omega_b^2(x)\}c^2,$$

$$b_1(x,s) = \{[s+v_c]\omega_b(x)\omega_p^2(x)\}^2 + \omega_p^4(x)[s+v_c]^4 + s^4\{[s+v_c]^2 + \omega_b^2(x)\}^2 + 2\omega_p^2(x)[s+v_c]^2 s^2\{[s+v_c]^2 + \omega_b^2(x)\}$$

$$b_2(x,s) = 2c^2\{[s+v_c]^2 + \omega_b^2(x)\}\{\omega_p^2(x)[s+v_c]^2 + s^2\{[s+v_c]^2 + \omega_b^2(x)\}\}$$

$$b_3(x,s) = c^4\{[s+v_c]^2 + \omega_b^2(x)\}^2.$$

After rearranging the terms and considering the lower limit of the integrals as  $x = x_0$ , ( $x_0$  is the starting point of medium '2'), the field components for  $p_1$  and  $p_2 = -p_1$  are obtained as

$$E_y(x,s) = j \frac{1}{4p_1(x,s)} \left\{ [a_2 p_1 + a_1] e^{\int_{x_0}^x p_1(\xi,s) d\xi} - [-a_2 p_1 + a_1] e^{-\int_{x_0}^x p_1(\xi,s) d\xi} \right\} \quad (19)$$

and

$$E_z(x, s) = \frac{1}{4p_1(x, s)} \left\{ [a_2 p_1 + a_1] e^{\int_{x_0}^x p_1(\xi, s) d\xi} - [-a_2 p_1 + a_1] e^{-\int_{x_0}^x p_1(\xi, s) d\xi} \right\}. \quad (20)$$

The magnetic field of the whistler-mode wave is obtained from the Maxwell's equations as,

$$H_y(x, s) = \frac{p_{1,2}(x, s)}{\mu_0 s} E_z(x, s), \quad (21)$$

$$H_z(x, s) = -\frac{p_{1,2}(x, s)}{\mu_0 s} E_y(x, s). \quad (22)$$

Substituting the values of  $E_y(x, s)$  and  $E_z(x, s)$ , we obtain<sup>22</sup>

$$H_y(x, s) = \frac{1}{4\mu_0 s} \left\{ [a_2 p_1 + a_1] e^{\int_{x_0}^x p_1(\xi, s) d\xi} - [-a_2 p_1 + a_1] e^{-\int_{x_0}^x p_1(\xi, s) d\xi} \right\}, \quad (23)$$

$$H_z(x, s) = -j \frac{1}{4\mu_0 s} \left\{ [a_2 p_1 + a_1] e^{\int_{x_0}^x p_1(\xi, s) d\xi} - [-a_2 p_1 + a_1] e^{-\int_{x_0}^x p_1(\xi, s) d\xi} \right\}. \quad (24)$$

Considering only forward propagating terms of field component, and substituting  $p_1(\omega) = -jK_1(\omega)$ ,  $s = j\omega$  the field components are rewritten as,

$$E_{zw}(x, \omega) = \frac{1}{4K_1(\omega)} [a_2(\omega)K_1(x, \omega) + ja_1(\omega)] e^{-j \int_{x_0}^x K_1(\xi, \omega) d\xi} = E_{z0}^+ e^{-j \int_{x_0}^x K_1(\xi, \omega) d\xi},$$

and

$$H_{yw}(x, \omega) = -\frac{K_1(x, \omega)}{\mu_0 \omega} E_{z0}^+ e^{-j \int_{x_0}^x K_1(\xi, \omega) d\xi}. \quad (25)$$

In a low loss medium ( $\nu_c \ll \omega$ ), the spectral Poynting vector is assumed to be constant<sup>16</sup>, and hence we can write

$$S \sim (E_{zw})(H_{yw})^* = (E_{z0}^+)^2 \frac{n_1(x)}{Z_0} \equiv \text{const} \equiv (A_0^+)^2, \quad (26)$$

where  $(H_{yw})^*$  is the complex conjugate of  $H_{yw}$ ,  $n_1(x)$  is the refractive index of the medium,  $Z_0$  is the wave impedance for vacuum and  $A_0^+(\omega)$  contains the unknown initial conditions characterizing the influence of the excitation.

The final form of the field components is obtained by solving the mode coupling equations at the boundary surface  $A_1$ , which separates medium '2' containing inhomogeneous plasma and medium '1' which is plasma-free medium containing the excitation source. Considering that the modes arising in the medium are not changed<sup>23</sup>, we obtain

$$\begin{aligned} -E_{1yR} &= jZ_0 H_{2yW} + jH_{2yN}, \\ -E_{1zG} + E_{1zR} &= Z_0 H_{2yW} + H_{2yN}, \\ E_{1zG} + E_{1zR} &= E_{2zW} + E_{2zN}, \\ E_{1yR} &= jE_{2zW} - jE_{2zN}; \end{aligned} \quad (27)$$

where subscripts R, W, N and G denoted for reflected mode, whistler mode, non-whistler mode and mode directly generated from source-current respectively. Representing the excitation source by a Dirac delta function  $\bar{J}_1(x, t) = I_{x0}\delta(x)\delta(t)$  and using the constancy of Poynting vector in a weakly inhomogeneous medium, we obtain the whistler-mode signal propagating through an inhomogeneous magnetoplasma as<sup>22</sup>,

$$E_{2z\omega}(x, t) = -\frac{Z_0}{4\pi} \int_{\omega_{\min}}^{\omega_{\max}} I_{x0}(\omega) \sqrt{\frac{K_1(x_0, \omega)}{K_1(x, \omega)}} \frac{k_0(\omega)}{k_0(\omega) + K_1(x_0, \omega)} e^{j \left[ \omega t - \int_{x_0}^x K_1(\xi, \omega) d\xi \right]} d\omega,$$

and

$$H_{2y\omega}(x, t) = \frac{1}{4\pi} \int_{\omega_{\min}}^{\omega_{\max}} I_{x0}(\omega) \sqrt{\frac{K_1(x, \omega)}{K_1(x_0, \omega)}} \frac{K_1(x_0, \omega)}{k_0(\omega) + K_1(x_0, \omega)} e^{j \left[ \omega t - \int_{x_0}^x K_1(\xi, \omega) d\xi \right]} d\omega, \quad (28)$$

where  $I_{x0}(\omega)$  is the amplitude of excitation current,

$$k_0 = \frac{\omega}{c}, \text{ and}$$

$$K_1(x, \omega) = k_0 \sqrt{1 - \frac{\{\omega - \nu_c\} \omega_p^2(x)}{\omega^2 \{[\omega - \nu_c] + \omega_b(x)\}}}$$

in simplified form.

The above result for two-component plasma (the effects of the motion of ions are also taken into account) for a lossless medium consisting of electron and proton reduces to:

$$E_{2zew}(x, t) = -\frac{Z_0}{4\pi} \int_{\omega_{\min}}^{\omega_{\max}} I_{x0}(\omega) \sqrt{\frac{k_1(x_0, \omega)}{k_1(x, \omega)}} \frac{k_0(\omega)}{k_0(\omega) + k_1(x_0, \omega)} \exp \left[ j \left[ \omega t - \int_{x_0}^x k_1(\xi, \omega) d\xi \right] \right] d\omega, \quad (29)$$

and

$$E_{2zpw}(x, t) = -\frac{Z_0}{4\pi} \int_{\omega_{\min}}^{\omega_{\max}} I_{x0}(\omega) \sqrt{\frac{k_3(x_0, \omega)}{k_3(x, \omega)}} \frac{k_0(\omega)}{k_0(\omega) + k_3(x_0, \omega)} \exp \left[ j \left[ \omega t - \int_{x_0}^x k_3(\xi, \omega) d\xi \right] \right] d\omega, \quad (30)$$

where subscript *e* is used for electron whistler and *p* is used for proton whistler.

$$k_1(x, \omega) = k_0(\omega) \sqrt{1 + \frac{\{\omega_p^-(x)\}^2}{\omega \{\omega_b^-(x) - \omega\}} - \frac{\{\omega_p^+(x)\}^2}{\omega \{\omega_b^+(x) + \omega\}}},$$

and

$$k_3(x, \omega) = k_0(\omega) \sqrt{1 + \frac{\{\omega_p^+(x)\}^2}{\omega \{\omega_b^+(x) - \omega\}} - \frac{\{\omega_p^-(x)\}^2}{\omega \{\omega_b^-(x) + \omega\}}},$$

where,  $\omega_p^-, \omega_b^-$  are electron's plasma frequency and gyro-frequency of the electron respectively, whereas plasma frequency and gyrofrequency of the proton are represented by  $\omega_p^+$  and  $\omega_b^+$  respectively.

## Computational technique

The above formalism is used to evaluate the dynamic spectrum of whistler-mode waves propagating longitudinally through the terrestrial atmosphere. We have chosen the case of terrestrial atmosphere because measured dynamic spectra under different conditions are available and we can easily compare the measured and numerically simulated results and validate the technique used in the evaluation of the electric fields as a function of space and time.

In evaluation of the above expression, we require electron density and magnetic field distribution along the path of integration (propagation). For the magnetic field we have taken dipole variation of terrestrial geomagnetic field; however, the diffusive equilibrium model DE-1 is considered for the electron density distribution<sup>24</sup>, with appropriate parameters, viz. electron density, electron temperature and ion abundance ratio like  $N(O^+) = 90\%$ ,

$N(He^+) = 2\%$  and  $N(H^+) = 8\%$  at reference height (750 km), where the signal is supposed to enter in to the magnetosphere. At the reference height, the particle number density ( $N_{ref}$ ) and electron temperature ( $T_{ref}$ ) are taken from the satellite-observed data<sup>25</sup>. The integration along the path of propagation is carried out using Simpson quadrature integration method.

In this manner, the electric field is calculated for the whole frequency range ( $0 < \omega < \omega_b$ ) for each frequency component separately. For evaluation of the dynamic spectrum, we have used the basic theory of signal processing. Concentrating on sampling theorem, discrete Inverse Fast Fourier transforms of  $N$  frequency points are computed to get the temporal variation of the wave field. We take the original vector of data  $f_j$  and rearrange it into bit-reversed order, so that the individual numbers are in the order not of  $j$  but the number obtained by bit-reversing  $j$ . We combine adjacent pairs to get two-point transforms, then combine adjacent pairs of pairs to get four-point transforms, and so on, until the first and the second halves of the whole data-set are combined and the final transform is obtained. Each combination takes of the order of  $N$  operations, and there are evidently  $\log_2 N$  combinations, so that the whole algorithm is of the order of  $\log_2 N$ .

Furthermore, the dynamic spectrum of signal or time-frequency mapping involves mapping of a signal (i.e. a one-dimensional function of time) into an image (i.e. a two-dimensional function of time and frequency) that displays the temporal localization of the spectral components of the signal. Therefore, to derive the dynamic spectrogram of the signal we have used Short Term Fourier Transform (STFT) technique, which involves chopping of the signal into short pieces, and then Fast Fourier Transform (FFT) is carried out piecewise. Moreover, STFT represents a sort of compromise between time- and frequency-based views of a signal. It provides information about both when and at what frequencies a signal event occurs, although this information can be only obtained with limited precision; the precision is determined by the size of the window, which is governed by the uncertainty principle.

## Simulated results

### Whistlers

Figure 2a shows the dynamic spectra of whistlers computed from full-wave model for Varanasi ( $L = 1.07$ ), Nainital ( $L = 1.17$ ) and Gulmarg ( $L = 1.28$ ). The dispersion of the wave depends upon path length, magnetic field and electron-density distribution along the path of propagation. Hence it varies from station to station. The zero frequency dispersion of the computed spectra is calculated and found as 5.8, 13.8 and 25.6 s<sup>1/2</sup> corresponding to Varanasi, Nainital and Gulmarg respectively. The dispersion is calculated for the magnetospheric path only, which is twice

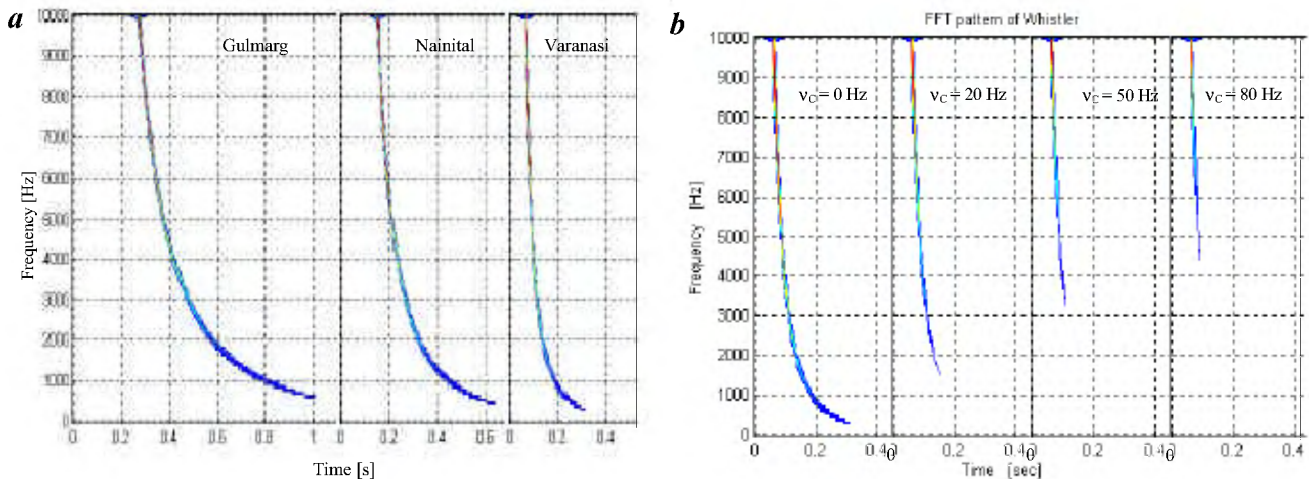


**Figure 2.** *a*, Dynamic spectra of whistler-mode signal simulated for Varanasi, Nainital and Gulmarg. *b*, FFT spectrum of computed whistlers for Varanasi with different inter-particle collision frequencies.

the dispersion produced during propagation from the reference height to the equator. In this computation dispersion produced during ionospheric path is not taken into account. The dispersion of observed whistlers at Varanasi, Nainital and Gulmarg is 12, 19 and  $24 \text{ s}^{1/2}$  respectively<sup>26,27</sup>. If the correction is made for the ionospheric path of propagation<sup>26,28</sup>, then the observed dispersion value reduces to 5, 11 and  $17 \text{ s}^{1/2}$  for Varanasi, Nainital and Gulmarg respectively. This shows that the simulated whistlers resemble closely to those observed at the low-latitude Indian stations.

The dynamic spectra shown in Figure 2 *b*, provide the simulated results for lossless as well as lossy medium for Varanasi. Instead of space-dependent collision frequency ( $\nu_c$ ) we have calculated for three constant collision frequencies, viz.  $\nu_c = 20, 50$  and  $80 \text{ Hz}$ . From Figure 2 *b* it is noted that the lower frequency part of the spectrum disappears showing that the effect of collision is not equally strong for the whole frequency range considered. We also note that when the collision frequency becomes appreciable, then at low latitudes whistler waves could appear as sferics because of larger attenuation at lower frequencies. Thus low-latitude whistler waves propagating during the conditions of enhanced collisions may appear as sferics. The major part of the propagation path of low-latitude whistlers lies in the upper ionosphere, where field-aligned plasma irregularities are abundantly present which affect the propagation of the VLF waves through the processes such as scattering, reflection, absorption, etc. To decipher these processes, simultaneous measurements of VLF waves and electron density fluctuations should be carried out.

### Nose whistlers

The dynamic spectra of whistler-mode waves when extended to higher frequencies exhibit a nose-like spectrum. Usually

group delay time decreases with increase in frequency. At a certain frequency, group delay time becomes minimum and further increase in frequency increases the group delay time. The frequency at which group delay time becomes minimum is known as nose frequency. Whistler recorded in India does not show appearance of nose frequency, which plays an important role in the whistler analysis, especially in the determination of the path of propagation. In the absence of nose frequency on the dynamic spectrum, extension methods are used to estimate nose frequency and hence path of propagation of recorded whistler<sup>14,29</sup>. Nose extension method developed for the analysis of whistlers is not suitable for the whistlers recorded at low-latitude stations, because nose frequency lies in the range of hundred kHz whereas the observed dynamic spectra mostly lie in the frequency range 1–10 kHz. Because of the errors introduced in the estimation of nose frequency, low-latitude whistlers are seldom used for probing the medium. We have applied full wave analysis and simulation technique to study the properties and observability of the nose frequency of non-nose whistlers recorded at low-latitude stations.

In this technique, the electron density, electron temperature and  $L$ -values are fixed by comparing the observed dynamic spectrum<sup>28</sup> with theoretically evaluated spectrum in the lower frequency range. Then these input parameters are used to reproduce the full dynamic spectrum of the whistler, including nose frequency. Figure 3 *a* shows the simulated whistlers with extended frequency range corresponding to whistlers recorded at Varanasi on the 9 March 1991. A clear variation in nose frequency is seen. It is found that the nose frequency increases with decrease in  $L$ -value<sup>30</sup>. Figure 3 *b* shows the effects of variation of electron number density on dispersion and nose frequency. Curve (ii) is simulated for electron number density  $n_e = 1.895 \times 10^4/\text{cm}^3$  at reference height, while curves (i) and (iii) are computed for 10% increment and decrement in  $n_e$ . Comparing these



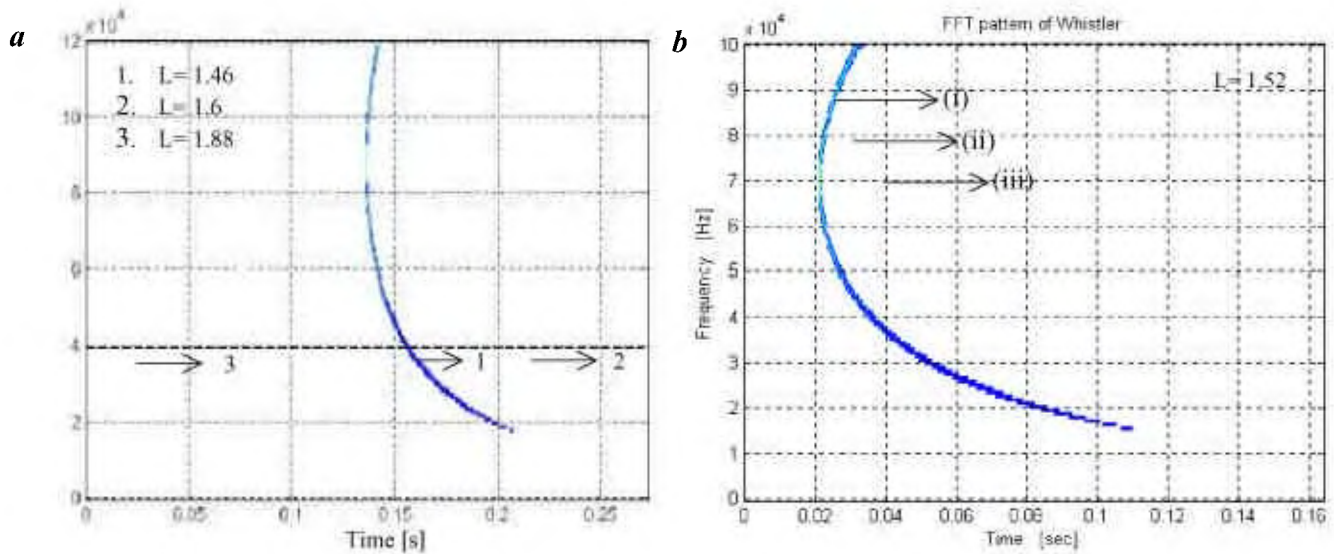


**Figure 3.** *a*, Simulated whistlers corresponding to observed whistlers at Varanasi<sup>2</sup> and extended to higher frequency range, including nose frequency. *b*, Dynamic spectra of simulated whistlers: (i) electron density increased by 10%, (ii) normal electron density  $n_{\text{ref}} = 1.895 \times 10^4 \text{ cm}^{-3}$ , and (iii) electron density decreased by 10%.

three curves of Figure 3 *b*, we find that the nose frequency  $f_n$  remains almost constant in all the three cases, as  $f_n$  depends only to a small extent on the ionization distribution<sup>31</sup>, while dispersion is different for curves *a*, *b* and *c*, which is calculated as 26.6, 25.9 and 25.1 respectively. Therefore, variation in the electron density along the path of propagation does not affect the nose frequency, although dispersion value changes<sup>32</sup>.

### Precursors

Precursors are riser-type signals observed on the dynamic spectrum preceding two-hop whistlers<sup>33</sup>, which are supposed to be triggered in some way by energy from the same lightning discharges that caused the accompanying whistler. The triggering mechanism remains unexplained because precursors exhibit several properties that are difficult to reconcile with available theories of generation mechanism. We have used the concept of parametric reflection to explain the dynamic spectra of precursors<sup>34</sup>.

In parametric reflection, a signal propagating in whistler mode along the geomagnetic field line may get reflected when the wave frequency becomes equal to the lower hybrid resonance frequency<sup>35</sup> ( $f_{\text{LHR}}$ ) which is given by

$$\frac{1}{\omega_{\text{LHR}}^2} = \frac{1}{\omega_{bi}^2 + \omega_{pi}^2} + \frac{1}{\omega_{bi}\omega_{be}},$$

where  $\omega_{bi}$ ,  $\omega_{pi}$  are gyrofrequency and plasma frequency of ions, while  $\omega_{be}$  is gyrofrequency of electrons.

In the case of dipolar geomagnetic field geometry, as the signal propagates towards the equator it encounters decreas-

ing magnetic field and, hence it is likely that the lower hybrid resonance reflection condition may be satisfied near the equator. Due to the symmetry of the dipole field, we find that there are two regions for the parametric reflection of a ducted whistler signal of a fixed frequency, which are situated symmetrically relative to the equatorial plane (Figure 4 *a*). The whistler, partially reflected from  $L_1$  level, produces a falling tone spectrum, whereas part of the signal partially reflected from  $L_2$  has a rising tone spectrum forming a hook-like shape on the spectrogram.

The whistler signal contains a frequency band and hence the whole signal will be reflected back from a range of arc length along the path of propagation, depending upon the lower and upper cut-off in the frequency of whistler wave packet. Thus, reflection point for different frequencies should be considered different. To make the computation simpler we have considered that the whole signal is compressed at  $f = 5 \text{ kHz}$  and accordingly, the reflection point is concentrated in a small arc length specified by  $f_{\text{LHR}} = 5 \text{ kHz}$ . However, in real situation, the reflection coefficient will be frequency-dependent, which is not considered in the present case.

Figure 4 *b* shows the dynamic spectra of reflected signal from  $L_1$ ,  $L_2$  and two-hop whistler for  $L = 2.0$  and  $f_{\text{LHR}} = 5 \text{ kHz}$ . The reflected signal from  $L_1$ , resembles the fractional-hop whistler, whereas the rising or precursor-type signal reflected from  $L_2$  lies between 0.63 and 0.89 s. The corresponding two-hop whistler lies between 0.95 and 1.22 s. The dispersion of precursor's dynamic spectrum changes as the location of  $L_2$  along the field line changes. If the reflection takes place from a point closer to the equator then the dispersion decreases, whereas if the reflection point moves away from the equator then dispersion increases.

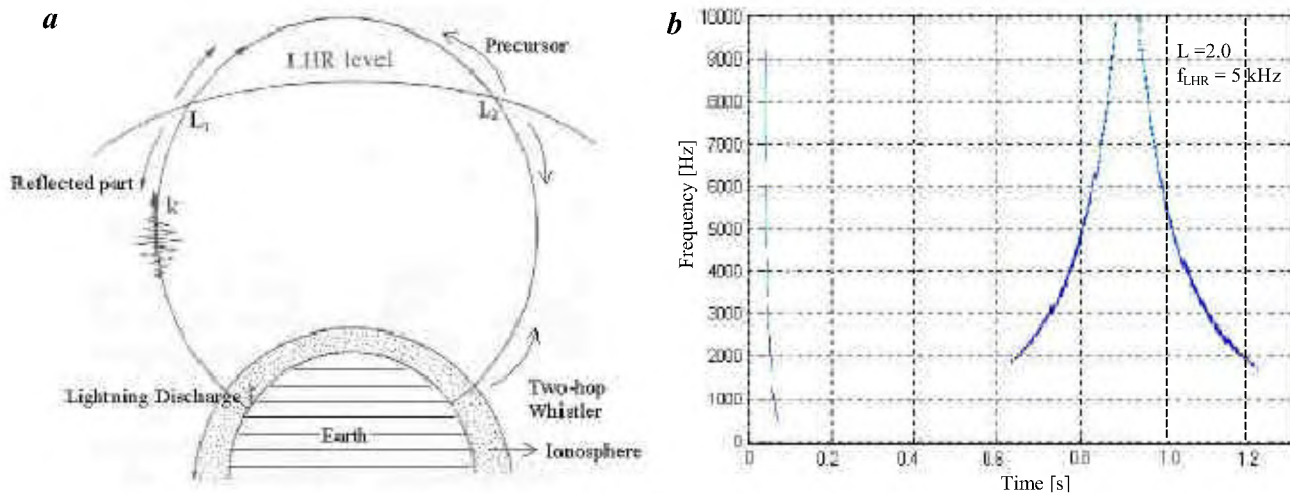


**Figure 4.** *a*, Schematic diagram illustrating reflection of whistler-mode wave at lower hybrid resonance level. *b*, Simulated dynamic spectra for fractional-hop whistler, precursor and two-hop whistler for  $L = 2.0$  and  $f_{LHR} = 5.0$  kHz.

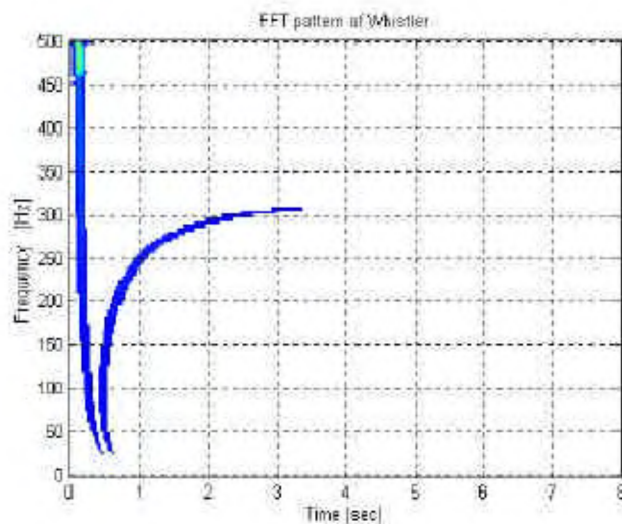


**Figure 5.** Dynamic spectra of electron and proton whistler clearly depicting the enhancement of group time delay at  $\omega = \omega_{bi}$ .

The shape of the spectrogram can also be obtained from group time delay considerations. Arrival time for different frequency components is evaluated separately and time versus frequency plot gives the spectrograms. The group time delay for the signal reflected from  $L_1$  can be written as<sup>34</sup>,

$$T_{R1} = 2 \int_0^{L_1} \frac{ds}{v_g(s)}, \text{ while } T_{R2} = 2 \int_0^{L_2} \frac{ds}{v_g(s)},$$

where  $v_g$  is the group velocity of whistler wave,  $ds$  is the path length along the geomagnetic field line, and  $L_1$  and  $L_2$  are the locations of parametric reflection at the lower hybrid resonance frequency  $f_{LHR}$ .

Calculated group time delay  $T_{R1} = 0.05$ ,  $T_{R2} = 0.90$  and  $T_{\text{two-hop}} = 0.94$  s at frequency  $f = 10$  kHz, while computed time delays from dynamic spectrum are  $T_{R1} = 0.05$ ,  $T_{R2} = 0.89$  and  $T_{\text{two-hop}} = 0.95$  s at the same frequency.

From computed time delays,  $T_{R2} \cong T_{\text{two-hop}} - T_{R1}$ , which confirms that reflection levels  $L_1$  and  $L_2$  are symmetrically situated on both sides of the equator (Figure 4*a*). It is also seen from the dynamic spectra that the time between causative sferic and precursor at any frequency is greater than that between the precursor and the two-hop whistler at the same frequency<sup>36</sup>. However, the delay between the sferic and trigger point of the precursor is greater than the delay between the trigger point and whistler at the same frequency<sup>37</sup>.

### Proton whistler

VLF wave observation on-board rockets and satellites shows simultaneous presence of right-hand and left-hand polarized mode. Right-hand polarized mode is known as electron whistler, whereas left-hand mode is known as proton whistler. To explain the dynamic spectrum of proton whistlers, it was assumed that the right-hand polarized wave modes transforms partly or entirely to left-hand polarized ion-cyclotron whistlers as they pass through the crossover region<sup>17</sup>. However, the process of mode conversion and its efficiency are not properly known. In the present case, we consider that the proton whistlers arise as a result of wave propagation through multi-component plasma. The presence of ions facilitates the propagation of left-hand mode.

In the case of multi-component plasma, right-hand polarized mode propagates in the frequency range  $0 < \omega < \omega_{be}$ , whereas left-hand polarized mode propagates in the frequency range  $0 < \omega < \omega_{bi}$  and group velocity for the two modes are different. Thus one obtains two dynamic spectra corresponding to electron and proton whistler mode (Figure 5). It is noted that as  $\omega$  approaches to  $\omega_{bi}$ , group velocity becomes quite small leading to large values for travel time. A small change in wave frequency causes large change in travel time. This is clearly visible in the spectrum of the proton whistler.

## Summary

In conclusion, we have successfully modelled the dynamic spectra of whistler-mode waves by solving Maxwell's equations using full wave theory. The computational method incorporating simulation technique produces whistlers, precursors, nose whistlers, and proton whistlers observed at ground stations in India, and hence it offers a more realistic description of different wave modes present in the magnetoplasma. Moreover, detailed analysis further determines the path of propagation which mainly lies in the ionosphere and in the inner magnetosphere, where the plasma processes are quite different and geomagnetic field lines are found to be more curved compared to mid/high latitudes. The influence of weak inhomogeneity along the path of propagation is included and by considering the collision frequency (collisions between electrons and neutrals), we have accounted for losses in dispersive media. It is encouraging to note that all the above described phenomena are simulated with the same computational code and with the help of same input parameters.

In the present method, plasma density and temperature distribution in the magnetosphere play a significant role and hence accurate measurements/models would give more reliable parameters of the wave and medium. Further, we have considered parallel propagation which is a limiting factor because, in real situation, waves may propagate with certain wave normal angle. In such a situation our model is not valid. However, we are in the process of developing the mathematical model and computations for finite wave normal angle.

1. Singh, R. P., Whistler studies at low latitudes: A review. *Indian J. Radio Space Phys.*, 1993, **22**, 139–155.
2. Singh, R. P., Singh, A. K. and Singh, D. K., Plasmaspheric parameters as determined from whistler spectrograms: A review. *J. Atmos. Sol. Terr. Phys.*, 1998, **60**, 495–508.
3. Barkhausen, H., Zwei mit Hilfe der neuen Verstärker entdeckte Erscheinungen. *Phys. Z.*, 1919, **20**, 401–403.
4. Eckersley, T. L., Note on musical atmospheric disturbances. *Philos. Mag.*, 1925, **49**, 1250–1259.
5. Barkhausen, H., Whistling tones from the earth. *Proc. IRE*, 1930, **18**, 1155–1159.
6. Storey, L. R. O., An investigation of whistling atmospherics. *Philos. Trans. R. Soc. London, Ser. A*, 1953, **246**, 113–141.
7. Helliwell, R. A., *Whistlers and Related Ionospheric Phenomena*, Stanford University Press, Stanford, California, 1965.
8. Al'pert, Y., 40 years of whistlers. *J. Atmos. Terr. Phys.*, 1980, **42**, 1–20.
9. Hayakawa, M. and Tanaka, Y., On the propagation of low latitude whistlers. *Rev. Geophys. Space Phys.*, 1978, **16**, 111–125.
10. Lalmani and Singh, R. P., Whistler occurrence rate with geomagnetic latitude. *J. Sci. Res., BHU*, 1978, **28**, 317–325.
11. Singh, B. and Hayakawa, M., Propagation modes of low- and very-low-latitude whistlers. *J. Atmos. Sol. Terr. Phys.*, 2001, **63**, 1133–1147.
12. Ohta, K., Nishimura, Y. and Kitagawa, T., Study of propagation characteristics of very low latitude whistlers by means of three-dimensional ray-tracing computations. *J. Geophys. Res.*, 1997, **102**, 7537–7546.
13. Budden, K. G., Lectures on magnetoionic theory. In *Geophysics, The Earth's Environment*, Gordon and Breach, New York, 1968.
14. Bernard, L. C., A new nose extension method for whistlers. *J. Atmos. Terr. Phys.*, 1973, **35**, 871–880.
15. Hamar, D., Tarcsei, G., Lichtenberger, J., Smith, A. J. and Yearby, K. H., Fine structure of whistlers recorded digitally at Halley, Antarctica. *J. Atmos. Terr. Phys.*, 1990, **52**, 801.
16. Ferencz, O., Whistler-mode propagation: Solution in homogeneous and weakly inhomogeneous lossy plasmas. *Period. Polytech. Electr. Eng.*, 1994, **38**, 267–285.
17. Gurnett, D. A., Shawhan, S. D., Brice, N. M. and Smith, R. L., Ion-cyclotron whistlers. *J. Geophys. Res.*, 1965, **70**, 1665–1688.
18. Kamke, E., Differentialgleichungen, Lösungsmethoden und Lösungen I, Akademische Verlagsgesellschaft, Geest and Porting K.G., Leipzig, (Punkt **23.5**), 1956, pp. 412–415.
19. Kamke, E., Differentialgleichungen, Lösungsmethoden und Lösungen II, Akademische Verlagsgesellschaft, Geest and Porting K.G., Leipzig, (Punkt **11.1**), 1965, pp. 93–98.
20. Budden, K. G., *Radio Waves in the Ionosphere*, Cambridge Univ. Press, London, 1966.
21. Ferencz, Cs., Electromagnetic wave propagation in inhomogeneous media: Strong and weak inhomogeneities. *Acta Tech. Acad. Sci. Hung.*, 1977, **85**, 433.
22. Singh, K., Singh, R. P. and Ferencz, O. E., Simulation of whistler mode propagation for low latitude stations. *Earth Planets Space*, 2004, **56**, 979–987.
23. Ferencz, Cs., Electromagnetic wave propagation in inhomogeneous media: Method of inhomogeneous basic modes. *Acta Tech. Acad. Sci. Hung.*, 1977, **86**, 79.
24. Park, C. G., Methods of determining electron concentration in the magnetosphere from nose whistlers, Tech. Report No. 3454, Radio-science Lab., Stanford University, Stanford, California, 1972, pp. 11–17.
25. Kelley, M. C., *The Earth's Ionosphere: Plasma Physics and Electrodynamics* (eds Dmowska, R. and Holton, J. R.), Academic Press, USA, 1989.
26. Somayajulu, V. V., Rao, M. and Tantry, B. A. P., Whistlers at low latitude. *Indian J. Radio Space Phys.*, 1972, **1**, 102–118.
27. Singh, R. P., Singh, U. P., Singh, A. K. and Singh, D. P., A case study of whistlers recorded at Varanasi. *Earth Planets Space*, 1998, **50**, 1–8.
28. Singh, R. P., Lalmani and Singh, U. P., Electron density distribution derived from low latitude whistler studies. *Ann. Geophys.*, 1993, **11**, 1011–1017.
29. Tarcsei, G., Strangeways, H. J. and Rycroft, M. J., Error sources and travel time residuals in plasmaspheric whistlers interpretation. *J. Atmos. Terr. Phys.*, 1989, **51**, 249–258.
30. Angerami, J. J. and Carpenter, D. L., Whistler studies of the plasmopause in the magnetosphere. (2) Electron density and total tube electron content near the knee in magnetospheric ionization. *J. Geophys. Res.*, 1966, **71**, 711–725.
31. Smith, R. L. and Carpenter, D. L., Extension of nose whistler analysis. *J. Geophys. Res.*, 1961, **66**, 2582–2586.
32. Singh, K., Singh, R. P., Singh, A. K. and Singh, R. N., Simulation of nose whistlers: An application to low latitude whistlers. *Planet. Space Sci.*, 2004 (communicated).
33. Singh, K. and Singh, R. P., Study of precursors using full wave analysis. *J. Atmos. Terr. Phys.*, 2004 (communicated).
34. Trakhtengerts, V. Y. and Rycroft, M. J., A new parametric reflection mechanism for ducted whistlers and an explanation of precursors. *J. Atmos. Terr. Phys.*, 1997, **59**, 1865–1871.
35. Stix, T. E., *The Theory of Plasma Waves* (ed. Nierenberg, W. A.), McGraw Hill, New York, 1962.
36. Laaspere, T. and Wang, C. Y., Whistler precursors. *Radio Sci.*, 1968, **3**, 213–218.
37. Dowden, R. L., Trigger delay in whistler precursors. *J. Geophys. Res.*, 1972, **77**, 695–699.

ACKNOWLEDGEMENT. K.S. thanks CSIR for financial assistance. The work is partly supported by DST (under SERC project), New Delhi.

Received 12 October 2004; revised accepted 23 February 2005